Facile growth of mesoporous Co_3O_4 nanowire arrays on Ni foam for high performance electrochemical capacitors

Fang Zhang[a], Changzhou Yuan[b], Xiangjun Lu[a], Luojiang Zhang[a], Qian Che[a], Xiaogang Zhang[a],*

[a] College of Material Science and Engineering, Nanjing University of Aeronautics and Astronautics, Nanjing 210016, PR China
[b] School of Materials and Engineering, Anhui University of Technology, Maanshan 243002, PR China

ARTICLE INFO

ABSTRACT

Mesoporous Co_3O_4 nanowire (NW) arrays freely standing on Ni foam substrate are prepared *via* two-step strategy: precipitating hydroxides followed by calcinating process. The slim Co_3O_4 NWs with average diameter of about 80 nm and length up to 10 μm are observed by transmission electron microscopy and scanning electron microscopy. Cyclic voltammetry, chronopotentiometry, and electrochemical impedance measurements are applied to investigate the performance of the Co_3O_4 NW arrays. Electrochemical tests show that Co_3O_4 NW arrays deliver a specific capacitance (SC) of 1160 F g^{-1} at 2 A g^{-1}, and even 820 F g^{-1} at 20 A g^{-1}. Also, the SC degradation is only 9.6% after 5000 continuous charge–discharge cycles at 8 A g^{-1}, indicating their excellent electrochemical stability. The improved performance is reasonably ascribed to their unique 3D hierarchical structure.

© 2011 Elsevier B.V. All rights reserved.

1. Introduction

Recently, Co_3O_4 has been widely investigated as a pseudocapacitive material with an anticipation that it could serve as a replacement for the expensive RuO_2, due to its practical availability, environmentally benign nature and lower cost [1–5]. Various nanostructured Co_3O_4 powders including nanoparticles [6], nanorods [7], nanotubes [8], and nanosheet-based microspheres [9] have been used in electrochemical capacitors (ECs). However, such ECs often result in low specific capacitances (SCs) and poor rate capability because the active materials are typically too insulating to support fast electron transport required by high rates [10]. Therefore, it is crucial to enhance charge transfer kinetics to fully utilize the redox reactions for high performance ECs. An effective way is to fabricate one-dimensional (1D) electroactive materials on current-collecting substrates, which can provide fast ion and electron transfer as well as sufficient effective area between electrolyte ions and active materials for Faradaic reactions [11–13]. Gao et al. synthesized 1D solid Co_3O_4 NWs (250 nm wide) on Ni foam by the ammonia-evaporation-induced method which showed a maximum SC of 746 F g^{-1} at 0.3 A g^{-1} [14,15]. More recently, Tu's group fabricated hollow Co_3O_4 NW arrays (200 nm wide) by seed-mediated hydrothermal method that showed a SC of 599 F g^{-1} at 2 A g^{-1} with 18% capacitance loss after 7500 cycles [16]. In com-

parison to the conventional Co_3O_4/carbon/PTFE electrode, these nanostructures can improve the contact between electroactive materials and current collectors which facilitates better kinetics. Unfortunately, the observed SCs are much less than its theoretical value (3560 F g^{-1}), particularly, at high rates. Thus, it is significant further tailoring the size and pore structure of Co_3O_4 NW to improve the electrochemical utilizations of Co_3O_4 at large current densities [12,17].

In this work, 1D mesoporous Co_3O_4 NW arrays have been successfully grown on Ni foam *via* a facile two-step method. The employed precursor is $Co(OH)_{1.10}Cl_{0.2}(CO_3)_{0.35} \cdot 1.74H_2O$, which on thermal treatment is transformed into spinel Co_3O_4. The mesoporous Co_3O_4 NWs and three-dimensional (3D) network architecture of Ni substrate composed a unique 3D hierarchical structure, which delivered large SCs and good electrochemical stability at high rates.

2. Experimental

2.1. Preparation of mesoporous Co_3O_4 NW arrays

Typically, 0.95 g of $CoCl_2 \cdot 6H_2O$ and 1.20 g of $CO(NH_2)_2$ were dissolved in 50 mL of water under stirring. Nickel foam (2 cm × 4 cm) was etched with 6 M HCl for 15 min to remove the oxide layer and then washed thoroughly with deionized water and absolute ethanol. Then, the homogeneous solution and the pretreated Ni foam were transferred into a Teflon-lined stainless steel autoclave. The autoclave was sealed and maintained at 95 °C for 8 h. After

* Corresponding author. Tel.: +86 025 52112902; fax: +86 025 52112626.
  E-mail address: azhangxg@163.com (X. Zhang).

cooled to room temperature, the nickel foam coated with pink precursors were rinsed under ultrasonication, and dried at 60 °C for 6 h. Finally, the precursors were converted to Co_3O_4 by annealing in air at 250 °C for 1 h. In average, the mass of Co_3O_4 NWs loaded on Ni substrate is 2.9 mg cm^{-2}, carefully weighted after the calcination treatment.

2.2. Characterization

The morphologies and structures of the samples were examined by scanning electron microscopy (SEM, LEO, 1430VP, Germany), high-resolution transmission electron microscopy (HRTEM) and selected area electron diffraction (SAED) (FEI, TECNAI-20). The crystallographic phases of as-prepared samples were investigated using powder X-ray diffraction (XRD, Bruker D8 with Cu K$_\alpha$ radiation) with a scanning rate of 3° min^{-1}. Thermal gravimetric analysis (TGA, NETZSCH STA 409) measurements were carried out at a heating rate 10 °C min^{-1} in air atmosphere. Fourier transform infrared (FT-IR) spectrum of the sample was recorded with a Nicolet 750 FT-IR spectrophotometer. N_2 adsorption/desorption was determined by Brunauer–Emmett–Teller (BET) measurements using an ASAP-2010 surface area analyzer.

Electrochemical measurements were carried out in a beaker cell with 6 M KOH aqueous solution as the electrolyte. The electrochemical performance of the Co_3O_4 NW arrays was studied by means of cyclic voltammetry (CV), chronopotentiometry (CP) and electrochemical impedance spectroscopy (EIS) measurements in a three-electrode half-cell system. The Co_3O_4 NWs growing on Ni foam (1 cm × 1 cm) was directly used as working electrode. A platinum plate (1 cm^2) and an Hg/HgO electrode were used as counter and reference electrodes, respectively. The SC values determined from the CP curves were calculated according to the following equation:

$$C_s = \frac{It}{m\Delta V} \tag{1}$$

where C_s, I, t, m and ΔV are SC (F g^{-1}), the discharge current (mA), the discharging time (s), the mass of the electroactive material (mg), and the potential interval of the discharge (V), respectively. The galvanostatic charge–discharge tests of the hybrid Co_3O_4-AC supercapacitor were performed in a two-electrode cell. All of the above electrochemical measurements were carried out on a CHI660C electrochemical workstation (Chenhua, Shanghai).

3. Results and discussion

3.1. Structural characterizations

Fig. 1 shows the XRD patterns of the NW products before and after calcination. Before heating, except for the peaks originating from the Ni substrate (marked by ▼), these diffraction peaks can be assigned to the precursor of cobalt chloride carbonate hydroxide (Co(OH)$_{1.10}$Cl$_{0.2}$(CO$_3$)$_{0.35}$·1.74H$_2$O, JCPDS No. 38-0547) [18]. It is demonstrated that Co(OH)$_{1.10}$Cl$_{0.2}$(CO$_3$)$_{0.35}$·1.74H$_2$O has a layered structure consists of positively charged Co–OH layers and counteranions located between the Co–OH layers, which can be easily converted into Co_3O_4 without evident nanostructure deformation [19]. After following heat treatment, the crystallinity of the product increased. All the diffraction peaks can be indexed to spinel Co_3O_4 (JCPDS No. 42-1467). No other peaks of impurities are observed, indicating that the cobalt hydroxide precursor was completely transformed to Co_3O_4 after calcination.

Fig. 2 presents the FT-IR spectra of the cobalt chloride carbonate hydroxide and Co_3O_4 samples, ranging from 4000 to 400 cm^{-1}, respectively. For the cobalt hydroxide precursor (Fig. 2a), the strong peak at about 3500 cm^{-1} is attributed to the stretching vibration
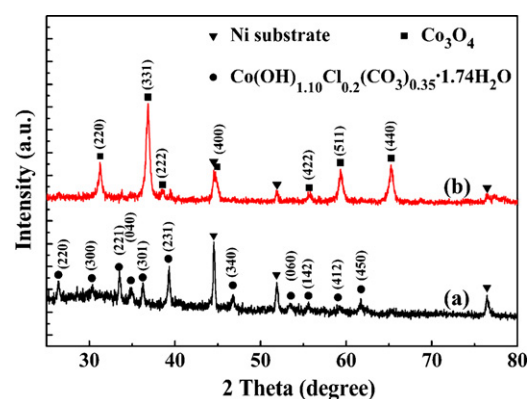

Fig. 1. XRD patterns of the NWs scraped off from Ni foam obtained by (a) hydrothermal treatment and (b) calcined at 250 °C.

of the O–H group of molecular water and hydrogen-bound O–H groups [20–22], ν(O–H). The weak band at 1625 cm^{-1} is due to the bending mode of water molecules. The presence of CO_3^{2-} in the sample is evidenced by its vibration bands from middle to lower wavenumbers. The bands observed at 1506, 1070, 831, 742, and 692 cm^{-1} are assigned to the stretching vibration ν(OCO$_2$), ν(C=O), δ(CO$_3$), δ(OCO), and ρ(OCO) [22], respectively, while the band at 962 cm^{-1} is ascribed to δ(Co–OH) bending modes and the band at 512 cm^{-1} is ascribed to ρ_w(CoOH) vibration [23]. As a comparison, the IR spectrum of the Co_3O_4 sample (Fig. 2b) shows no absorptions of CO_3^{2-} and Cl$^-$ anions, which indicate that the anions in the as-prepared precursor have been completely removed. Two distinctive bands at 663 and 576 cm^{-1} are the characteristics of the Co–O stretching vibrations in Co_3O_4 [24]. In addition, the weak adsorptions at 3424 and 1630 cm^{-1} correspond to the bending and stretching vibration modes of absorbed water molecules on the surface. The above analysis revealed that the temperature of 250 °C is high enough for complete decomposition of the precursor into Co_3O_4 phase.

The thermal behavior of the as-prepared precursor was investigated using a TGA technique (Fig. 3). The TGA curve indicates that the weight loss of the cobalt hydroxide precursor is ca. 4.0% below 200 °C, which could be ascribed to the removal of absorbed water molecular. From 200 to 350 °C, the weight loss is mainly attributed to the loss of structure water by dehydroxylation and the release of CO_2 and HCl gases produced by decomposition of anions, which is ca. 21.6%, roughly in agreement with the expected value (22.5%) on the basis of the decomposition reaction (Eq. (2)). The last weight loss (ca. 4.7%) after 300 °C may be due to a continuous thermal depletion of deep-trapped hydroxyl groups [25]. The total weight loss is ca. 30.3%, which is less than the theoretical value of 41.4%,
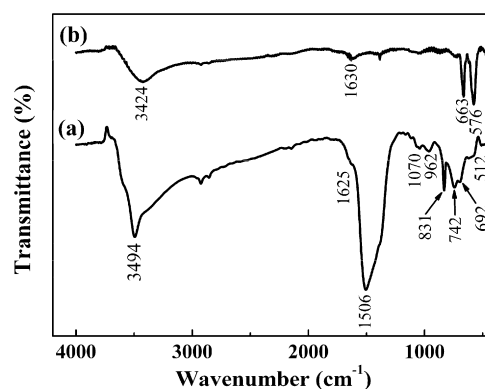

Fig. 2. FT-IR spectra of the (a) cobalt hydroxide and (b) Co_3O_4 samples.
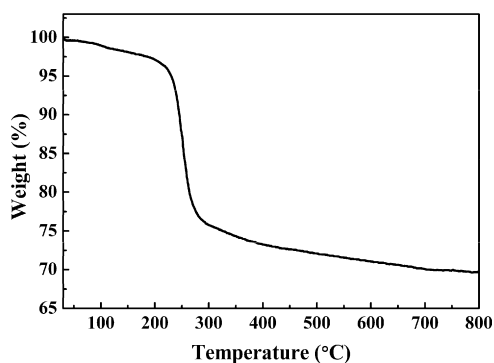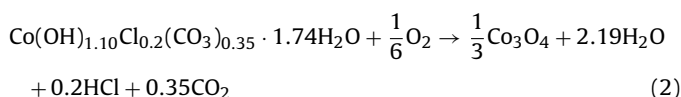
Fig. 3. TGA curve of the cobalt hydroxide precursor.

the mismatch between the observed and expected loss is mainly due to the adsorbed water [18].

$$Co(OH)_{1.10}Cl_{0.2}(CO_3)_{0.35} \cdot 1.74H_2O + \frac{1}{6}O_2 \rightarrow \frac{1}{3}Co_3O_4 + 2.19H_2O$$

$$+ 0.2HCl + 0.35CO_2 \qquad (2)$$

The morphologies and structures of as-obtained Co_3O_4 samples were investigated by SEM and HRTEM. Fig. 4a–c shows the SEM images of Co_3O_4 NW arrays viewed from the top. It can be seen that Co_3O_4 NWs with high density (Fig. 4a) were grown uniformly on the Ni foam, forming a 3D hierarchical structure (inset in Fig. 4a). The NWs with sharp tips are homogeneously aligned and are separated apart adequately (Fig. 4b and c). The main length of the NWs is *ca.* 10 μm along the growth direction (Fig. 4c). One can also see that the Co_3O_4 NWs grow almost vertically from the substrate. Furthermore, the adhesion of the NWs on the substrate is

strong considering the fact that the sample had been ultrasonicated for tens of minutes before the SEM examination. Fig. 5a exhibits a typical TEM image of a single NW scraped off from Ni substrate, from which we can clearly see that the diameter of the single NW is around 80 nm and many mesopores are widely distributed on the surface. The lattice spacing of 0.285 nm is corresponded to the (2 2 0) crystal planes of spinel Co_3O_4, as seen from the HRTEM image (Fig. 5c), which is consistent with the XRD data. The SAED pattern (Fig. 5d) demonstrates a polycrystalline structure of the Co_3O_4 NW.

To gain further insight into the porous structure and pore size distribution of the Co_3O_4 NWs, BET measurements were performed to examine its textural properties. As shown in Fig. 6, it can be seen that the Co_3O_4 NWs sample give rise to type-IV isotherms, according to IUPAC classification. At a relative pressure of above 0.7, the distinct hysteresis loop reflects the capillary condensation of the mesopores [26–28]. Barrett–Joyner–Halenda (BJH) pore size distribution calculated using the adsorption curve in the context of the BJH method further confirms the mesoporous structure with pore size of 9.7 nm. The mesoporosity is assigned to the thermal decomposition of the starting material, which could result in weight loss and volume shrinking. Moreover, the Co_3O_4 NWs exhibit high BET surface area of 74.9 m^2 g^{-1} and large pore volume of 0.25 cm^3 g^{-1}. Such characteristics of the as-prepared cobalt oxide sample permit easy access for ions to the electrode/electrolyte interfaces, which is crucial for surface redox reactions [16,29].

3.2. Electrochemical measurements

Fig. 7a shows the CV curves of the Ni foam supported-Co_3O_4 NW arrays and pure Ni foam at a scan rate of 0.5 mV s^{-1}. Two pairs of well-defined redox peaks (P_1/P_4 and P_2/P_3) indicate good pseudocapacitive characteristics of the Ni supported-Co_3O_4 NW arrays.

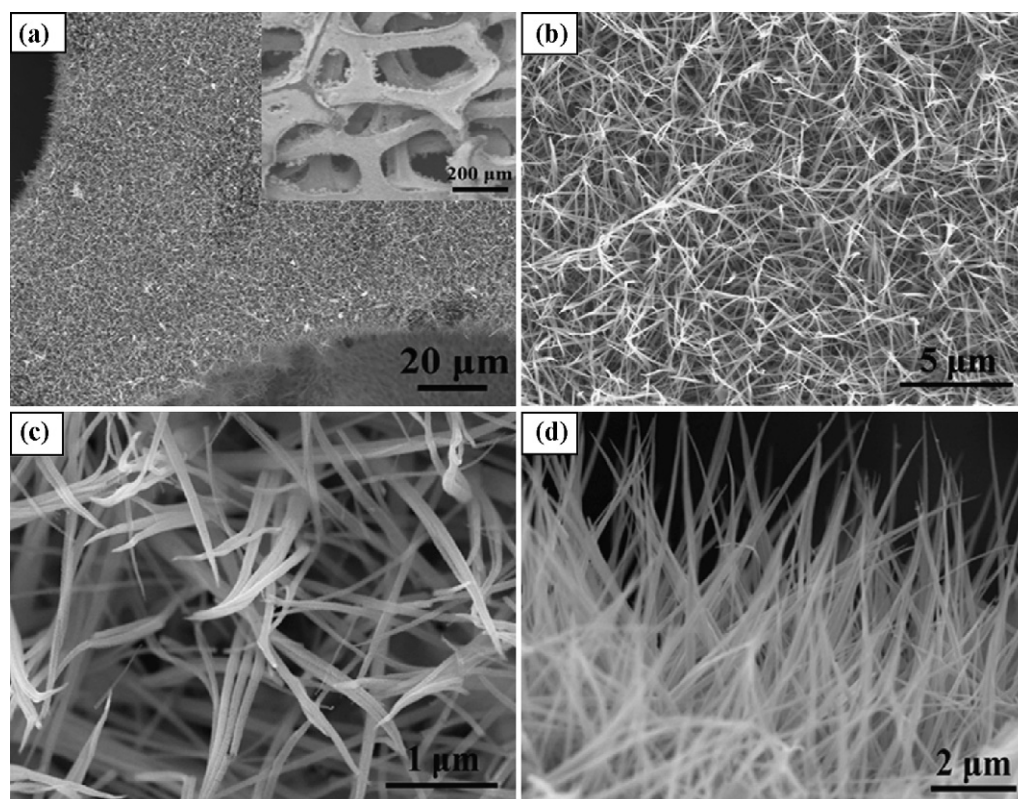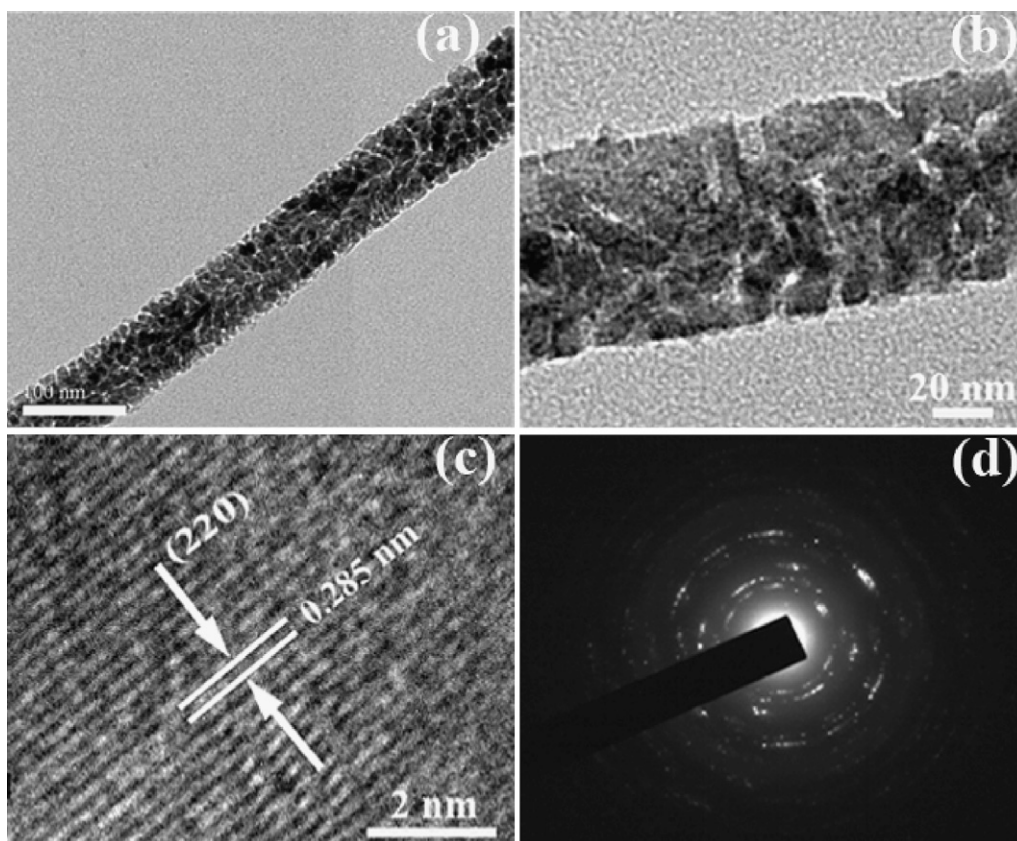**Fig. 4.** (a) Low-magnification SEM image of Co_3O_4 NW arrays viewed from the top and (b and c) locally enlarged images; the inset of (a) shows the 3D hierarchical structure of the Co_3O_4 NW arrays growing on Ni foam. (d) SEM image of Co_3O_4 NW arrays from the side view.

Fig. 5. (a) TEM image of a single Co_3O_4 NW. (b) Magnified TEM image reveals the mesoporous structure of the Co_3O_4 NW. (c) High resolution image of the NW with a d-spacing of 0.285 nm for the (2 2 0) plane and (d) the corresponding SAED pattern.
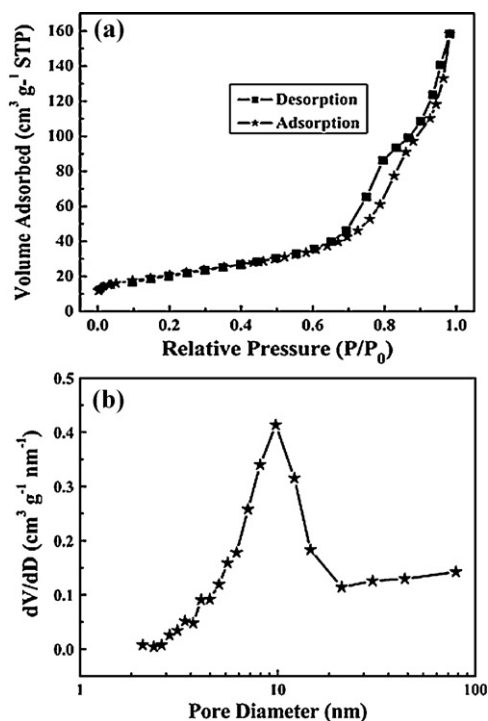
**Fig. 6.** (a) The gas (N_2) adsorption–desorption isotherm loop and (b) a histogram of the pore size distribution data for the cobalt oxide NWs after thermal treatment at 250 °C.

The peak of P_1/P_4 is ascribed to the conversion between Co_3O_4 and CoOOH, described as follows [30,31]:

$$Co_3O_4 + OH^- + H_2O \leftrightarrow 3CoOOH + e^- \qquad (3)$$
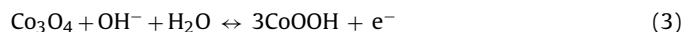
The redox peak of P_2/P_3 corresponds to the change between CoOOH and CoO_2, expressed as follows:

$$CoOOH + OH^- \leftrightarrow CoO_2 + H_2O + e^- \qquad (4)$$
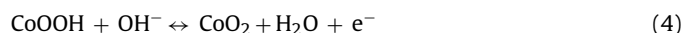
However, for the pure Ni foam as an electrode, the response current is relatively weak, which is negligible in contrast with that of the Co_3O_4 NW arrays. Because the capacitance is directly proportional to the area under the CV curve, the contribution from the Ni foam to the total capacitance is ignored in the following discussion. The CV curves recorded at high scan rates are presented in Fig. 7b. With increasing the scan rate, the redox peaks become broad and cathodic peaks overlap, indicating fast redox reactions occurred at electroactive material/electrolyte interfaces.

Fig. 7c shows the typical CP curves of the Co_3O_4 NW arrays at different current densities in the potential window of 0–0.5 V. The shape of charge–discharge curves is almost symmetrical in all cases, suggesting their high coulombic efficiency. The SCs of the Co_3O_4 NW arrays can be calculated based on the charge–discharge curves in Fig. 7c and the typical data collected in Fig. 7d. The Co_3O_4 NW arrays exhibited excellent pseudocapacitances of 1160 F g^{-1} at 2 A g^{-1}, 996 F g^{-1} at 5 A g^{-1}, 884 F g^{-1} at 10 A g^{-1}, 861 F g^{-1} at 15 A g^{-1} and 820 F g^{-1} at 20 A g^{-1}, respectively, and 71% capacity retention is obtained when the charge–discharge rate changes from 2 to 20 A g^{-1}. Our results are even better than previous reports, where Co_3O_4 NWs with solid (746 F g^{-1}) or hollow interiors (599 F g^{-1}) were synthesized by Gao et al. [14] and Xia et al. [16], respectively. In our case, the Co_3O_4 NWs have slim diameter and mesoporous structure, which can greatly reduce the pathways
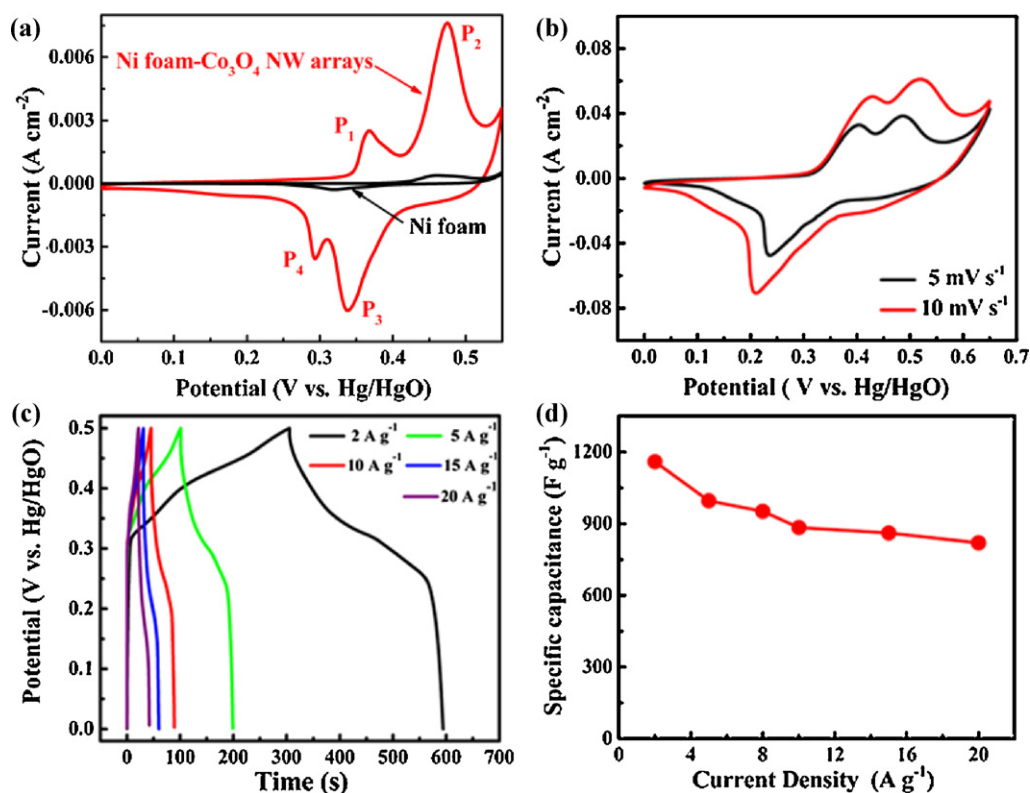
Fig. 7. (a) CV curves of Ni foam supported-Co$_3$O$_4$ NW arrays (red) and pure Ni foam (black) in the potential range of 0–0.55 V, respectively. (b) CV curves of the Co$_3$O$_4$ NW arrays at different scan rates of 5 and 10 mV s^{-1}. (c) CP plots and (d) the SCs of the Co$_3$O$_4$ NW arrays at different current densities. (For interpretation of the references to color in legend, the reader is referred to the web version of the article.)

for insertion and extrusion of OH$^-$ and provide more active surface area for Faradaic reactions [17,32], and consequently promote the pseudocapacitance. It suggests that such NW arrays with slim morphology and uniform mesoporosity favor high electrochemical utilization.

The cyclability of the Co$_3$O$_4$ NW arrays in 6 M KOH electrolyte is an important parameter for practical applications (as shown in Fig. 8). During the first 300 cycles, the SC increases from 962 F g^{-1} to 1040 F g^{-1}. This must result from the activation process of the Co$_3$O$_4$ electroactive material. Thereafter, it decreases to 940 F g^{-1} after the subsequent 4700 cycles. Such a low SC degradation of 9.6% after 4700 continuous cycles demonstrates the good electro-

Fig. 8. Cycling performance of the Co$_3$O$_4$ NW arrays at 8 A g^{-1}. The inset shows the last 20 cyclic charge–discharge curves.

chemical stability of the Co$_3$O$_4$ NW arrays at large current densities. The inset of Fig. 8 shows the last 20 charge–discharge cycles of the Co$_3$O$_4$ NW arrays. The morphology and structure changes after 5000 cycles were studied to understand the good cyclability of our electrode. The SEM and XRD data of the cycled electrode are depicted in Fig. 9. Fig. 9a is the SEM image of Co$_3$O$_4$ NW arrays electrode after 5000 charge–discharge tests. It can be observed that the NW arrays exhibit small bending deformation compared to the as-synthesized morphology. The NWs tend to cluster at their tips to form sheaflike structure, which may be due to the strong interaction forces between the long and thin NWs [33]. However, the electrode maintained its NW arrays structure after cycling test, maintaining the pathway for electrons and ions. Retaining the structure integrity is a key factor to ensure the cyclability of the material [11]. In addition, its XRD shape seen in Fig. 9b remains almost unchanged, matching that of the pristine electrode, indicating that the crystalline structure of the electrode is indeed preserved over the measured cycle life.

In order to investigate the detailed characteristics of a capacitive electrode, we carried out comparative studies using EIS measurements before and after cycling tests. Fig. 10 shows Nyquist plots of the Co$_3$O$_4$ NWs electrode measured over the frequency range of 0.01 Hz–100 kHz at the open circuit potential. Both EIS curves consist of a depressed arc in high frequency regions and an inclined line in low frequency regions. An equivalent circuit proposed to fit the spectra is shown as an inset of Fig. 10, where the R_s is the internal resistance, R_{ct} is Faradic charge transfer resistance, W is the Warburg impendance, and C_{dl} is the double layer capacitance. R_s is characterized by the high-frequency intercept on the real axis (Z'), which includes the resistance of the electrolyte, the ohmic resistance of the active materials and the contact resistance at the active materials/current collector interface [34–36]. As indicated in Fig. 10a, the value of R_s of the pristine electrode is 1.4 Ω. After
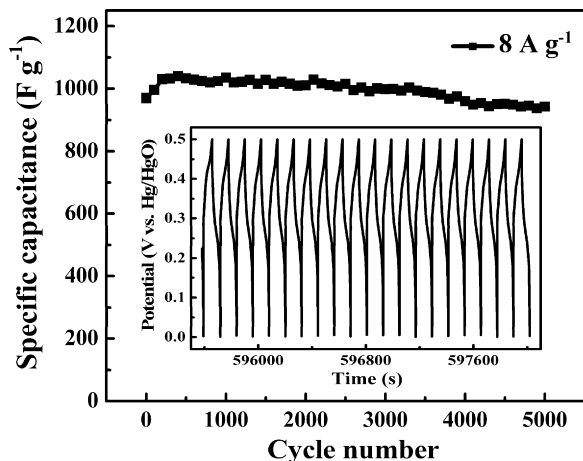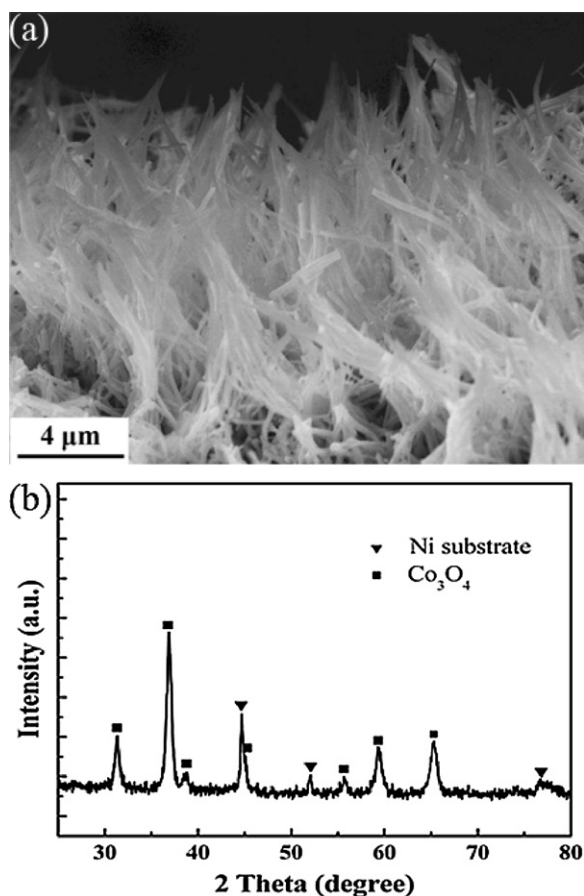
Fig. 9. (a) Typical SEM image and (b) XRD pattern and of the Co$_3$O$_4$ NW arrays electrode after 5000 continuous charge–discharge cycles.

Fig. 11. (a) Galvanostatic charging/discharging curves (I = 2 A g^{-1}) of the hybrid Co$_3$O$_4$-AC supercapacitor in 6 M KOH electrolyte. (b) Ragone plot of the specific energy and specific power at various charge–discharge rates.

5000 charge–discharge cycles, the R_s value has increased to 1.8 Ω, showing that the conductivity of the electrode decreases after long-term cycling. Besides, compared to the pristine electrode, the radius of the semi-circle for the 5000-cycled electrode has enlarged in medium frequency regions. Accordingly, the R_{ct} increases from *ca.* 1.6 Ω to *ca.* 2.5 Ω, which may be due to some morphological changes with cycles. As seen in Fig. 9a, the clustered NWs will reduce the electroactive surface area (a combination of the specific surface area and electrical conductivity) and block the path of ion diffusion to some extent, thereby hindering the charge transfer
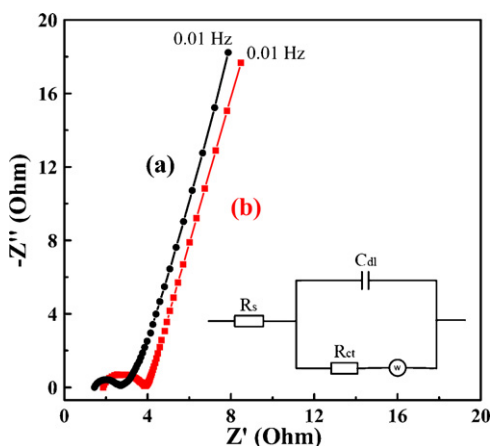
between the electrode surface and electrolyte. It is indicated that the charge transfer resistance is related to the electroactive surface area. The larger the electroactive surface area, the lower the charge transfer resistance [17]. At low frequency, two straight lines in the Nyquist plot incline at an angle of around 90° to the Z′-axis and this suggests good capacitive behavior [36].

To show the practical applications of the Ni supported-Co$_3$O$_4$ NW arrays, we fabricated a hybrid supercapacitor consisting of the Co$_3$O$_4$ NW arrays as the positive electrode and activated carbon (AC) as the negative electrode. The weight of AC is calculated using the following equation [37,38], $m_- = (C_{s,+}\Delta E_+)/(C_{s,-}\Delta E_-)m_+$, where ΔE is the potential range for the charge and discharge process and m is the mass of the electrode materials. On the basis of the SC values and potential ranges for the Co$_3$O$_4$ NW arrays and AC, the optimized mass loading of AC is 6.7 mg. Fig. 11a shows the galvanostatic charging/discharging curves of the Co$_3$O$_4$-AC hybrid supercapacitor at a current density of 2 A g^{-1} in the potential range from 0 to 1.5 V. As shown in Fig. 11a, a linear variation of the voltage was observed during the charging–discharging process, which can prove that the hybrid capacitor has a good capacitive behavior. The Ragone plot of Co$_3$O$_4$-AC supercapacitor illustrates the corresponding energy/power densities (Fig. 11b), which were calculated from galvanostatic charge–discharge data at various current densities. All the data were calculated on the basis of the total mass of active materials of two electrodes. The data of Fig. 11b clearly demonstrated that the hybrid supercapacitor based on Co$_3$O$_4$ NWs and AC has a good specific energy density and power density. Remarkably, the hybrid capacitor operated at 1.5 V is capable of delivering a high energy density of 37.8 Wh kg^{-1} and a high power density of 19.5 kW kg^{-1}. Compared to previously reported asymmetric capacitors [39–43], our hybrid capacitor display comparable energy density and higher power density, which can be attributed to the binder-free nature and 3D porous structure of the Co$_3$O$_4$ NWs electrode, which thus improves the power density of asymmetric cells.

Fig. 10. Nyquist plots of the Co$_3$O$_4$ NWs electrode (a) before and (b) after 5000 charge–discharge cycles. The inset is the equivalent circuit.
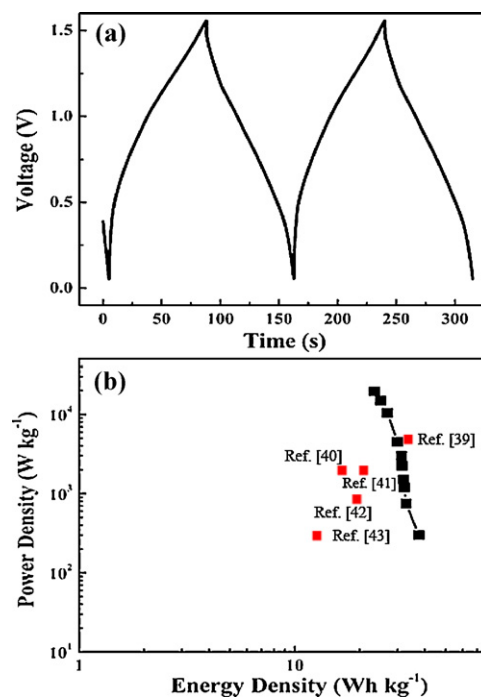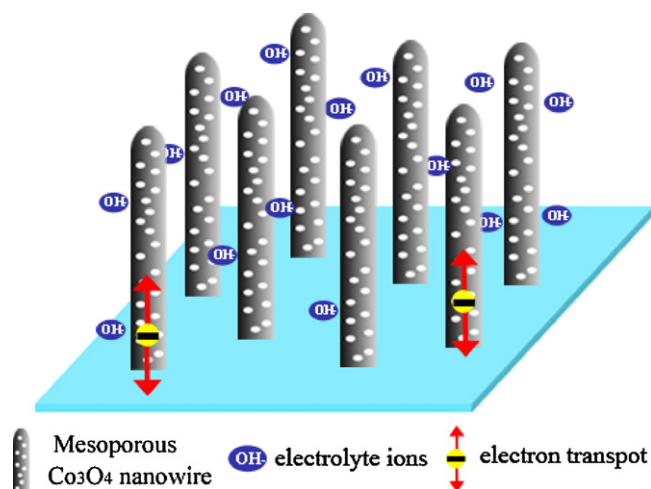
Fig. 12. Schematic representation of microstructure and energy storage characteristics of the Co_3O_4 NW arrays.

The superior pseudocapacitive performance of the Co_3O_4 NW arrays can be attributed to their unique 3D hierarchical structure, as shown schematically in Fig. 12. (1) 3D porous structure of the Ni foam substrate can facilitate the fast penetration of the KOH electrolyte and its contact with the surface of Co_3O_4 NWs, which has a significant positive effect on the electrochemical performance of Co oxide [44]; (2) each Co_3O_4 NW is connected directly on Ni skeleton, building up an express way for charge transfer. The slim diameter and mesoporous structure of the Co_3O_4 NWs will greatly reduce the OH^- ions diffusion length within Co_3O_4 phase, ensure its high electrochemical utilizations; (3) Co_3O_4 NWs growing directly on Ni foam can form a good adhesion and better electrical contact between Co_3O_4 and Ni substrate, which is beneficial to improve long-term cycling stability at high rates [45]. In addition, as the Co_3O_4 NW arrays are connected to Ni framework, the need for binders or conductive carbon, which add extra contact resistance or weight, is eliminated.

4. Conclusions

In summary, we have prepared mesoporous Co_3O_4 NW arrays growing on Ni foam *via* a facile two-step method. The Co_3O_4 NW arrays have shown high SCs and good cyclability. High SCs of $1160 F g^{-1}$ at $2 A g^{-1}$ and $820 F g^{-1}$ at $20 A g^{-1}$ were obtained by CP tests. More importantly, the electrode can still remain a SC of $940 F g^{-1}$ after 5000 continuous charge–discharge cycles at $8 A g^{-1}$. The outstanding electrochemical performance should be ascribed to good contact, short electron transporting paths, high surface-to-volume ratio, porous structures and open space in the unique electrode. The binder-free Co_3O_4 NW arrays electrode could be a promising candidate for ECs applications and the cost-effective synthesis strategy can be exploited to prepare other transition metal oxide nanostructures.

References

[1] M.B. Zheng, J. Cao, S.T. Liao, J.S. Liu, H.Q. Chen, Y. Zhao, W.J. Dai, G.B. Ji, J.M. Cao, J. Tao, J. Phys. Chem. C 113 (2009) 3887–3894.
[2] L.R. Hou, C.Z. Yuan, L. Yang, L.F. Shen, F. Zhang, X.G. Zhang, RSC Adv. 1 (2011) 1521–1526.
[3] Y. Wang, Z.Y. Zhong, Y. Chen, C.T. Ng, J.Y. Lin, Nano Res. 4 (2011) 695–704.
[4] Y. Liu, C.H. Mi, L.H. Su, X.G. Zhang, Electrochim. Acta 53 (2008) 2507–2513.
[5] X.H. Xia, J.P. Tu, X.L. Wang, C.D. Gu, X.B. Zhao, Chem. Commun. 47 (2011) 5786–5788.
[6] T.Y. Wei, C.H. Chen, K.H. Chang, S.Y. Lu, C.C. Hu, Chem. Mater. 21 (2009) 3228–3233.
[7] T. Zhu, J.S. Chen, X.W. Lou, J. Mater. Chem. 20 (2010) 7015–7020.
[8] J. Xu, L. Gao, J.Y. Cao, W.C. Wang, Z.D. Chen, Electrochim. Acta 56 (2010) 732–736.
[9] S.L. Xiong, C.Z. Yuan, X.G. Zhang, B.J. Xi, Y.T. Qian, Chem. Eur. J. 15 (2009) 5320–5326.
[10] H.L. Wang, H.S. Casalongue, Y.Y. Liang, H.J. Dai, J. Am. Chem. Soc. 132 (2010) 7472–7477.
[11] Y.G. Li, B. Tan, Y.Y. Wu, Nano Lett. 8 (2008) 265–270.
[12] Z.Y. Lu, Z. Chang, J.F. Liu, X.M. Sun, Nano Res. 4 (2011) 658–665.
[13] J. Jiang, J.P. Liu, R.M. Ding, J.H. Zhu, Y.Y. Li, A.Z. Hu, X. Li, X.T. Huang, ACS Appl. Mater. Interfaces 3 (2011) 99–103.
[14] Y.Y. Gao, S.L. Chen, D.X. Cao, G.L. Wang, J.L. Yin, J. Power Sources 195 (2010) 1757–1760.
[15] G.L. Wang, D.X. Cao, C.L. Yin, Y.Y. Gao, J.L. Yin, L. Cheng, Chem. Mater. 21 (2009) 5112–5118.
[16] X.H. Xia, J.P. Tu, Y.J. Mai, X.L. Wang, C.D. Gu, X.B. Zhao, J. Mater. Chem. 21 (2011) 9319–9325.
[17] M.S. Wu, Appl. Phys. Lett. 87 (2005) 153102–153104.
[18] Z.G. Zhao, F.X. Geng, J.B. Bai, H.M. Cheng, J. Phys. Chem. C 111 (2007) 3848–3852.
[19] H. Zhang, J.B. Wu, C.X. Zhai, X.Y. Ma, N. Du, J.P. Tu, D.R. Yang, Nanotechnology 19 (2008) 035711.
[20] L.H. Su, X.G. Zhang, C.H. Mi, B. Gao, Y. Liu, Phys. Chem. Chem. Phys. 11 (2009) 2195–2202.
[21] J.C. Villegas, O.H. Giraldo, K. Laubernds, S.L. Suib, Inorg. Chem. 42 (2003) 5621–5631.
[22] R. Xu, H.C. Zeng, J. Phys. Chem. B 107 (2003) 12643–12649.
[23] X.W. Xie, P.J. Shang, Z.Q. Liu, Y.G. Lv, Y. Li, W.J. Shen, J. Phys. Chem. C 114 (2010) 2116–2123.
[24] H.Y. Guan, C.L. Shao, S.B. Wen, B. Chen, J. Gong, X.H. Yang, Mater. Chem. Phys. 82 (2003) 1002–1006.
[25] S.M. Zhang, H.C. Zeng, Chem. Mater. 21 (2009) 871–883.
[26] H.L. Wang, Q.M. Gao, L. Jiang, Small 7 (2011) 2454–2459.
[27] J.G. Yu, G.H. Wang, B. Cheng, M.H. Zhou, Appl. Catal. B 69 (2007) 171–180.
[28] Y. Sakatani, D. Grosso, L. Nicole, C. Boissière, G.J. Soler-Illia, C. Sanchez, J. Mater. Chem. 16 (2005) 77–82.
[29] C.L. Xu, Y.Q. Zhao, G.W. Yang, F.S. Li, H.H. Li, Chem. Commun. (2009) 7575–7577.
[30] P.Y. Keng, B.Y. Kim, I.B. Shim, R. Sahoo, P.E. Veneman, N.R. Armstrong, H. Yoo, J.E. Pemberton, M.M. Bull, J.J. Griebel, E.L. Ratcliff, K.G. Nebesny, J. Pyun, ACS Nano 3 (2009) 3143–3157.
[31] C. Lin, J.A. Ritter, B.N. Popov, J. Electrochem. Soc. 145 (1998) 4097–4103.
[32] J. Li, Z. Tang, Z. Zhang, Chem. Mater. 17 (2005) 5848–5855.
[33] B. Liu, H.C. Zeng, J. Am. Chem. Soc. 125 (2003) 4430–4431.
[34] C.Z. Yuan, H. Dou, B. Gao, L.H. Su, X.G. Zhang, J. Solid State Electrochem. 12 (2008) 1645–1652.
[35] D.Y. Youn, H.L. Tuller, T.S. Hyun, D.K. Choi, I.D. Kim, J. Electrochem. Soc. 158 (2011) A970–A975.
[36] R. de Levie, Electrochim. Acta 8 (1963) 751–780.
[37] P.C. Chen, G.Z. Shen, Y. Shi, H.T. Chen, C.W. Zhou, ACS Nano 4 (2010) 4403–4411.
[38] V. Khomenko, E. Raymundo-Pinero, F. Béguin, J. Power Sources 153 (2006) 183–190.
[39] Y.G. Wang, L. Yu, Y.Y. Xia, J. Electrochem. Soc. 153 (2006) A743–A748.
[40] Q.T. Qu, P. Zhang, B. Wang, Y.H. Chen, S. Tian, Y.P. Wu, R. Holze, J. Phys. Chem. C 113 (2009) 14020–14027.
[41] Q.T. Qu, Y. Shi, L.L. Li, W.L. Guo, Y.P. Wu, H.P. Zhang, S.Y. Guan, R. Holze, Electrochem. Commun. 11 (2009) 1325–1328.
[42] Y.G. Wang, Y.Y. Xia, Electrochem. Commun. 7 (2005) 1138–1142.
[43] Q. Wang, Z.H. Wen, J.H. Li, Adv. Funct. Mater. 16 (2006) 2141–2146.
[44] M.J. Deng, F.L. Huang, I.W. Sun, W.T. Tsai, J.K. Chang, Nanotechnology 20 (2009) 175602.
[45] G.W. Yang, C.L. Xu, H.L. Li, Chem. Commun. (2008) 6537–6539.